Published in partnership with CSCP and USTB



https://doi.org/10.1038/s41529-025-00598-3

Effects of europium doping on thermal property and failure behaviour of $Gd_2Zr_2O_7$ thermal barrier coatings

Check for updates

Zaoyu Shen ⊠, Yuqing Luo, Guanxi Liu, Jianwei Dai, Limin He & Rende Mu⊠

This work concentrates on the phase, composition, thermo-physical properties, microstructure, service lifetime, and failure behaviour of GdEuZrO/YSZ thermal barrier coatings fabricated via electron beam-physical vapor deposition. The thermo-physical property of the GdEuZrO ceramics are superior to Gd₂Zr₂O₇ and YSZ due to the substitution of Eu. A feathery structure characterized by inner-gaps and linear pores is observable at the column tips. The GdEuZrO/YSZ TBCs have demonstrated the most extended service lifetime compared to YSZ or GdEuZrO TBCs. The high thermal expansion coefficient, the feathery microstructure, the low thermal conductivity, and the substitution effect of Eu are key contributors to the enhanced thermal durability of the TBCs. After the thermal cycling test, the outward migration of Ni, Cr, Co, Al, and Hf elements results in the emergence of Ni-Cr-Co-Al-Hf oxides. The migration of elements and the progression of cracks are identified as the primary causes of failure in the GdEuZrO/YSZ TBCs.

Thermal barrier coatings (TBCs) represent a vital and widespread thermal insulation technique utilized in gas turbine engines. TBCs are designed for high thermal and phase stability, resistance to corrosion, and are crafted from ceramic oxides that conduct heat minimally for turbine blades¹⁻³. Typically, TBCs are composed of one ceramic top layer, one metallic, and one intermediate layer of thermally grown oxide (TGO). The core purpose of TBCs is to shield metallic materials from oxidation and corrosion in the presence of high-temperature gases^{4,5}. To date, the predominant material utilized for TBCs is yttria partially stabilized zirconia (YSZ), containing 6-9 wt.% yttria. Processing YSZ ceramics necessitates advanced hightemperature capabilities due to their high melting points, which are close to 3000 K. Thermal plasma and electron beam are the primary energy sources for depositing TBCs⁶⁻¹⁰. Notably, the columnar structure characteristic of TBCs is attainable through electron beam-physical vapor deposition (EB-PVD) technology. This structure enhances the TBCs' ability to accommodate strain, allowing for enduring operation at high temperature⁸⁻¹². While TBCs are designed for high-temperature function, their main performance is thermal conductivity and lifetime at high temperature exceeding 1100 °C. However, YSZ TBCs are prone to sintering and degradation above 1200 °C due to the t'-phase instability¹³⁻¹⁵.

To overcome the limitations of YSZ TBCs, significant advancements have been focused on advanced ceramic oxides with low thermal conductivity. Among these materials, rare earth zirconates (RE-ZrO₂), pyrochlore/fluorite ceramics, and perovskite-structured oxides are under

consideration as potential successors to YSZ16-25. Particularly, gadolinium zirconate (Gd₂Zr₂O₇, GZ) ceramics have garnered considerable interest due to their high melting point, phase stability, matching thermal expansion coefficients, and reduced thermal conductivity²⁰⁻²⁵. However, GZ singlelayer coatings often demonstrate inadequate thermal cycling lifetime at temperatures exceeding 1100 °C. To enhance the thermal performance, the substitution of complex atomic structures of rare elements such as Cerium (Ce), Ytterbium (Yb), Erbium (Er), and Lanthanum (La) in the A or B sites of the GZ ceramics has been selected²⁰⁻³⁰. This elemental substitution introduces point defects into the crystal lattice, leading to a further reduction in thermal conductivity. Moreover, the shortcomings of single GZ layers can be overcome by designing multilayer or graded structures. Incorporating a YSZ ceramic middle layer above the metallic bottom layer allows for a broader range of thermal expansion coefficient mismatch with the substrate, resulting in reduced thermal stress between the top layer and the metallic bottom layer, thereby improving the thermal cycling lifetime³⁰⁻³⁵. Our previous work has explored and debated the criteria for choosing YSZ and RE-GZ coatings, focusing on their thickness ratios, porosity levels, and the characteristics of their columnar microstructures 14,17,36,37. This comprehensive analysis was crucial for understanding how these factors influence the overall performance of the coatings in terms of thermal insulation, mechanical resistance, and durability under high temperature conditions. Nevertheless, scientific and technological investigations into europium (Eu)-doped GZ ceramics and TBCs remain limited. The effects of Eu

Key Laboratory of Advanced Corrosion and Protection for Aviation Materials, Beijing Institute of Aeronautical Materials, Aero Engine Corporation of China, Beijing, 100095, China. 🖂 e-mail: shenzaoyu@163.com; murendeaecc@126.com

substitution on key performance characteristics - including thermal conductivity, thermal cycling lifetime, and failure mechanisms - require a comprehensive investigation and continue to pose significant challenges in the development of advanced TBC systems. Based on differences in atomic mass, ionic radius, interatomic bonding forces, and electronic configurations, europium (Eu) was selected as a partial substituent for gadolinium (Gd) sites in $Gd_2Zr_2O_7$ to enhance its thermophysical properties, particularly thermal conductivity and thermal expansion coefficient.

In this study, we present a double-layer TBCs system, comprising one GdEuZrO top layer and one YSZ bottom layer, and deposited using EB-PVD technology. The as-deposited TBCs feature a hierarchical structure that includes a feathery morphology with interspersed inner gaps and linear pores, which contribute to its enhanced performance. The extended lifetime can be attributed to the unique microstructure of the coating, which provides better resistance to thermal stress and the associated crack propagation. The result indicated that the GdEuZrO TBCs exhibit a relatively high thermal lifetime and good thermal conductivity compared with other multilayers, graded structures, bilayers, and other zirconates in the literature 10-18. Furthermore, this study delves into the relationship between crack formation and the evolution of the TGO layer within the TBCs system. The TGO layer, which forms at the interface between the ceramic top coat and the metallic bond coat, plays a pivotal role in the overall performance and failure mechanism of TBCs. The growth and thickening of the TGO layer can induce thermal stresses, leading to crack initiation and propagation. Understanding this relationship is essential for developing strategies to enhance the thermal cycling resistance and overall durability of TBCs. The insights gained from this study can guide future developments in TBC materials and deposition techniques, aiming to achieve even higher levels of performance and durability in demanding high-temperature environments.

Results and discussion Thermo-physical property and phase

In TBCs systems, the thermal conductivity of materials is recognized as a critical thermal attribute. Currently, a significant focus in ceramic research is the development of materials with low thermal conductivity, as these are highly desirable for thermal insulation and energy efficiency applications. Figure 1 illustrates the trend in thermal conductivity and thermal diffusivity for GE5Z, GE10Z, GE20Z, and YSZ ceramics as the temperature increases. It is observed that both the thermal conductivity and thermal diffusivity of the series of GEZ and YSZ decrease within the temperature range of 20-1000 °C. At 1000 °C, the thermal diffusivity of GE20Z ceramics is as low as 0.252 mm²/s, compared to 0.723 mm²/s for YSZ ceramics. When the temperature is raised to 1200 °C, the thermal diffusivity of GE20Z is 0.267 mm²/s, and for YSZ, it is 0.780 mm²/s. Notably, the thermal diffusivity of the series of GEZ ceramics is approximately 50% less than that of YSZ. As shown in Fig. 1b, the thermal conductivity of GE20Z at 1000 °C is only 0.889 W/mK, and it slightly increases to 1.089 W/mK at 1200 °C. In contrast, the thermal conductivity of YSZ ceramics is significantly higher, at 2.450 W/mK at 1000 °C and 2.662 W/mK at 1200 °C due to

the relatively low fractional porosity. The thermal conductivity of our YSZ bulk ceramics (ca. $2.5\,\mathrm{W/m\cdot K}$) falls within the range of values reported in previous literature $^{1.4.7}$. The series of GEZ ceramics exhibit a thermal conductivity that is nearly 50% lower than that of YSZ. These findings underscore that the series of GEZ ceramics are among the materials with low thermal conductivity, making them potentially superior candidates for applications in TBCs. The lower thermal conductivity of GEZ ceramics helps to minimize the heat transfer through the coating, thus protecting the underlying substrate from high temperatures.

In the field of TBCs, thermal conductivity is a pivotal attribute, predominantly governed by the scattering of phonons. This scattering is triggered by interactions among phonons themselves (phonon-phonon scattering), by material defects (phonon-defect scattering), and material's boundaries (phonon-boundary scattering)¹⁰⁻¹⁵. In ceramics with larger grain sizes, the impact of phonon-boundary scattering is often negligible, making phonon-phonon and phonon-defect scattering the dominant factors. The incorporation of the larger europium (Eu) cation into the GEZ lattice disrupts the fluorite structure, resulting in a shortened mean free path for phonons. This material, where Eu³⁺ replaces Gd³⁺, exemplifies a solid-state substitution with implications for thermal conductivity. The atomic mass and ionic radius discrepancies between Eu³⁺ (with an atomic mass of 151.96 and an ionic radius of 1.07 Å) and Gd³⁺ (with an atomic mass of 157.25 and an ionic radius of 1.05 Å) introduce point defects into the Gd₂Zr₂O₇ ceramic. These defects, primarily vacancies and substitutional impurities, significantly influence the material's thermal conductivity. Furthermore, the presence of Eu³⁺ in Gd₂Zr₂O₇ enhances the scattering efficiency of phonons, both between themselves and off defects. This enhanced scattering is the chief contributor to the reduced thermal conductivity observed in these ceramics. On the other hand, the O-Gd interatomic bonding force differs significantly from that of O-Eu^{38,39}. The electronic configurations of Eu and Gd also exhibit significant differences in their electron outside the nucleus arrangements (Eu: [Xe] $4 f^{0} 6 s^{2}$ and Gd: [Xe] $4 f^{0} 5 d^{1} 6 s^{2}$). These variations in interatomic bonding force and outer electron arrangements further contribute to the low thermal conductivity of GdEuZrO ceramic materials. Consequently, the low thermal conductivity of GEZ ceramics, which is a result of these factors, is particularly beneficial for TBCs applications, enhancing their performance and efficiency.

Based on the thermal durability results, the thermal expansion coefficient (TEC), ingot, and coating phase would focus on the GE10Z ceramic material. The introduction of rare earth elements is recognized for its significant impact on the thermal and physical properties of $Gd_2Zr_2O_7$ ceramic materials. In this work, we focus on the substitution of Eu for Gd site in $Gd_2Zr_2O_7$ ceramics. This substitution is expected to modulate the material's characteristics, potentially enhancing its performance in high-temperature applications. Figure 2a illustrates the XRD patterns of the GE10Z ingot and coating, which are compared against the standard pattern for $Gd_2Zr_2O_7$ (cubic fluorite structure, space group Fm-3m, PDF#80-0471). The presence of XRD peaks at 34.33°, 39.67°, 57.39°, and 68.50° corresponds to the (111), (200), (220), and (311) reflections of the $Gd_2Zr_2O_7$ standard, respectively.

Fig. 1 | Thermal diffusivity and thermal conductivity of YSZ, GZ, GE5Z, GE10Z, and GE20Z bulk ceramics. a thermal diffusivity; (b) thermal conductivity.

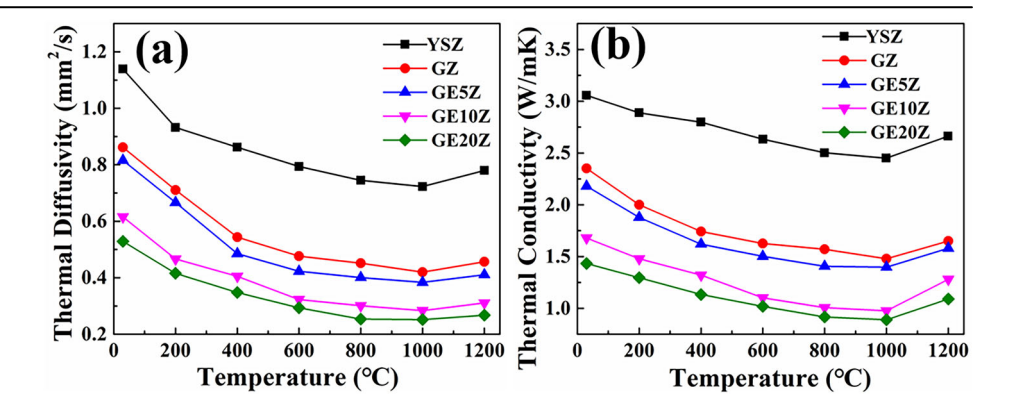


Fig. 2 | Phase structure and thermal expansion coefficient. a XRD patterns of GE10Z ingot and coating; (b) thermal expansion coefficient of YSZ, GE5Z, GE10Z and GE20Z bulk ceramics.

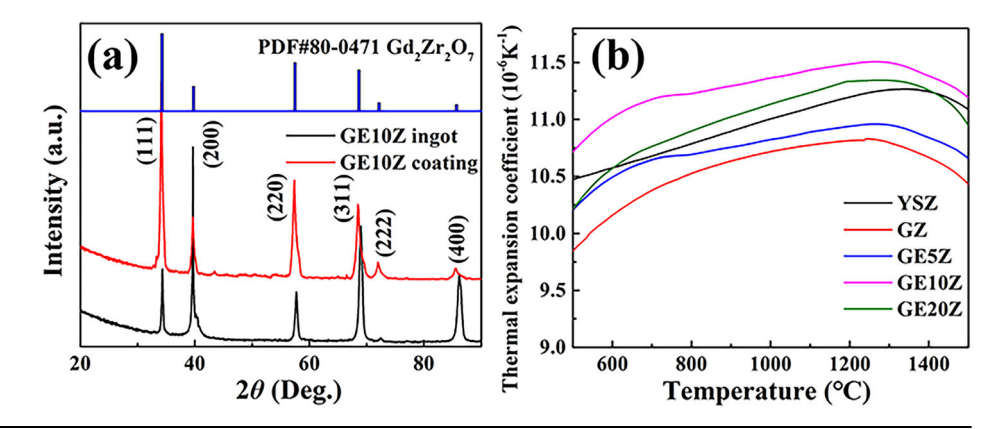
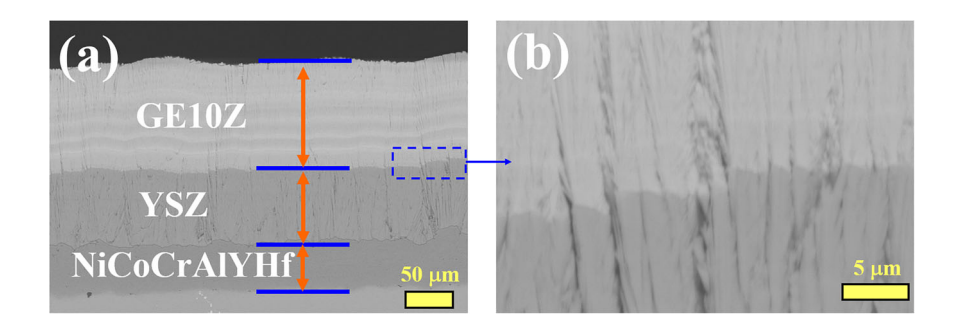


Fig. 3 | Microstructure of the as-deposited GE10Z/ YSZ TBCs. a cross-section; (b) YSZ/GE10Z interface.



This alignment confirms that the fluorite structure remains the primary phase in both the ${\rm GE10Z}$ ingot and coating.

As we know, TBCs are complex, multi-layer systems composed of a bond coat, a thermally grown oxide (TGO) layer, and a ceramic top coat. The thermal stability of TBCs during thermal cycling is a critical factor, as it is influenced by the varying thermal expansion coefficient (TEC) of the individual layers^{3–5}. Mismatches in TEC among the layers would lead to the generation of thermally induced residual stresses, which are a primary source of TBC failure. Given that the TEC values for the substrate and bond coat typically range from $16-19*10^{-6}$ and $15-16*10^{-6}$ K⁻¹, respectively, these are notably higher than those of the conventional ceramic top layers. Consequently, a ceramic top layer with a higher TEC might be more desirable to minimize the TEC discrepancy between layers.

At present, the dilatometer method is the predominant technique for measuring thermal expansion coefficients, offering a reliable means to assess these critical properties in TBC materials. Thus, the TEC can be determined by measuring the length changes as a function of temperature. Figure 2b illustrates the TEC values for YSZ, GZ, GE5Z, GE10Z, and GE20Z bulk ceramics bulk ceramics. In the temperature range of 500–1500 °C, the GE10Z ceramic material demonstrates exhibits the highest TEC (10.71 * $10^{-6}\,\mathrm{K}^{-1}$ to $11.19*10^{-6}\,\mathrm{K}^{-1}$) among YSZ, GZ, GE5Z and GE20Z. For temperatures between 500 and 1350 °C, the TEC of GE10Z consistently increases. However, beyond 1350 °C, there is a slight decrease in the TEC value for GE10Z. Specifically, from 1200 to 1500 °C, the TEC of GE10Z falls within the range of $11.49*10^{-6}\,\mathrm{K}^{-1}$ to $11.20*10^{-6}\,\mathrm{K}^{-1}$, surpassing that of YSZ, which ranges from $11.05*10^{-6}\,\mathrm{K}^{-1}$ to $11.20*10^{-6}\,\mathrm{K}^{-1}$. This suggests that GE10Z could be a more suitable material for applications where a higher TEC is advantageous.

Generally, the TEC is predominantly associated with the anharmonicity of phonons within lattice vibrations 40-42. This anharmonicity is influenced by the ionic radius and the field strength of the cationic species introduced, such as Europium (Eu). Replacing the smaller Gadolinium (Gd) cation (with a radius of 1.05 Å) with the Europium cation (1.07 Å), which is slightly larger, results in an increased average ionic radius at the A site. This increase subsequently reduces the Goldschmidt tolerance factor, which is

conducive to a higher TEC. Additionally, the incorporation of Eu into the Gd site introduces numerous point defects into the GE ceramic material, generating a stress field within the lattice. The elevated TEC of the GdEuZrO layer mitigates the stress caused by thermal expansion discrepancies between the ceramic top layer, the YSZ layer, the NiCoCrAlYHf layer, and the substrate.

Microstructure characterization

Figure 3 presents a SEM analysis of the cross-section of the as-deposited GE10Z/YSZ/NiCoCrAlYHf coatings. The TBCs system, as depicted in Fig. 3a, is composed of three distinct layers: one GE10Z top layer, one YSZ intermediate layer, one NiCoCrAlYHf bond coat, and the substrate. The SEM images reveal that the GE10Z top layer has a thickness ranging from approximately 100 to 120 µm. The YSZ intermediate layer is slightly thinner, with a thickness of about 70 to 85 µm, while the NiCoCrAlYHf bond coat is approximately 45 to 55 µm. Figure 3b illustrates the microstructure of the coatings, with the columnar grains measuring a diameter of roughly 3.0 to 5.0 µm. The interface between the GE10Z and YSZ layers appears free of significant defects, indicating a robust adherence. The columnar grains are observed to grow continuously through the YSZ layer and across the interfaces, both with the YSZ and the GE10Z layers, showcasing a seamless integration achieved during the EB-PVD process. This continuous growth pattern and the absence of defects at the interfaces are indicative of the high-quality bonding and material integrity within the TBCs system. Furthermore, the surface of as-deposited GE10Z coatings exhibit a pyramidlike surface microstructure without any horizontal cracks, as shown in Fig. S2.

In an effort to assess the distribution of elements across the GE10Z/YSZ/NiCoCrAlYHf TBCs, a comprehensive analysis was performed using EPMA. The EPMA maps not only corroborate the structural integrity of the three-layered TBCs system but also highlight the distribution of elements within each layer. The resulting maps, as presented in Fig. 4, offer a detailed visualization of the elemental composition within the cross-section of the TBCs. As shown in Fig. 4a, the TBCs exhibit a clear three distinct layers: an upper ceramic top layer, a middle ceramic layer, and a bottom metallic bond

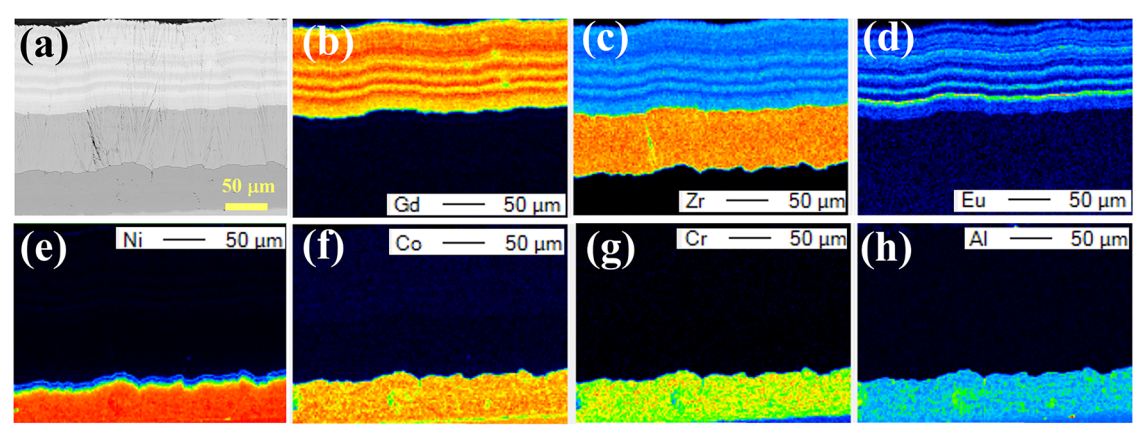


Fig. 4 | Cross-section and corresponding EPMA maps of the as-deposited GE10Z/YSZ/NiCoCrAlYHf TBCs. a cross-section; (b) Gd; (c) Zr; (d) Eu; (e) Ni; (f) Co; (g) Zr; (h) Al

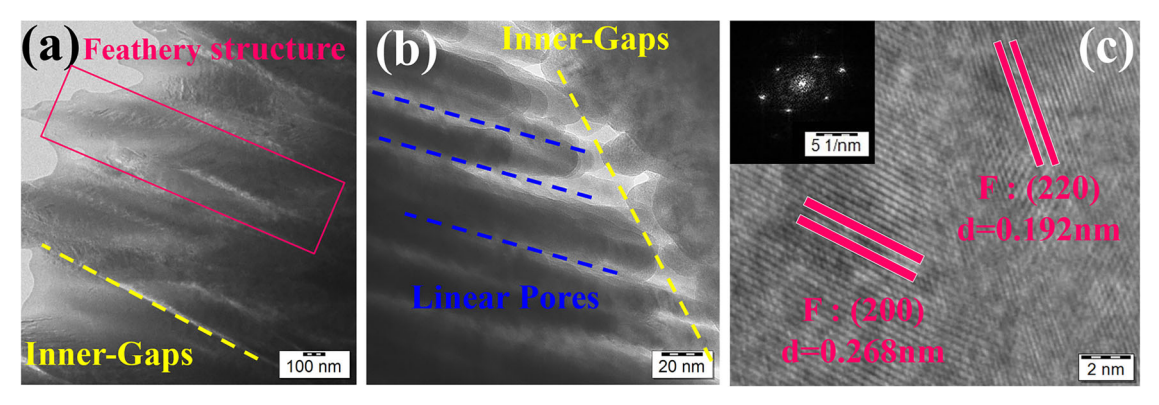


Fig. 5 | Microstructure of the as-deposited GE10Z layer. a TEM image of feathery structure; (b) TEM image of inner gaps; (c) HRTEM image and corresponding processed FFT image.

coat. The top layer, identified as the GdEuZrO layer, is characterized by a rich presence of Gd, Eu, and Zr. The GdEuZrO ingot is evaporated into the gas phase by electron beam energy in the EB-PVD process. The vapor cloud solidifies into a solid phase on the substrate. The difference of vapor pressure and melting points among the various elements (Gd₂O₃, Eu₂O₃, and ZrO₂) is sensitive to the electron beam energy leading to the Gd, Zr and Eu heterogeneously distributed throughout the coatings. Conversely, the bottom layer, which serves as the bond coat, is predominantly composed of Ni, Co, Cr, and Al, elements that are integral to the NiCoCrAlYHf layer. This layer plays a critical role in adhering the TBCs to the substrate and in withstanding the thermal stresses experienced in service. Furthermore, the absence of significant elemental gradation or intermixing at the interfaces between layers suggests a stable and coherent bond, which is vital for the long-term durability of the TBCs under the extreme conditions of thermal cycling and high-temperature exposure typical in aerospace and industrial gas turbine applications.

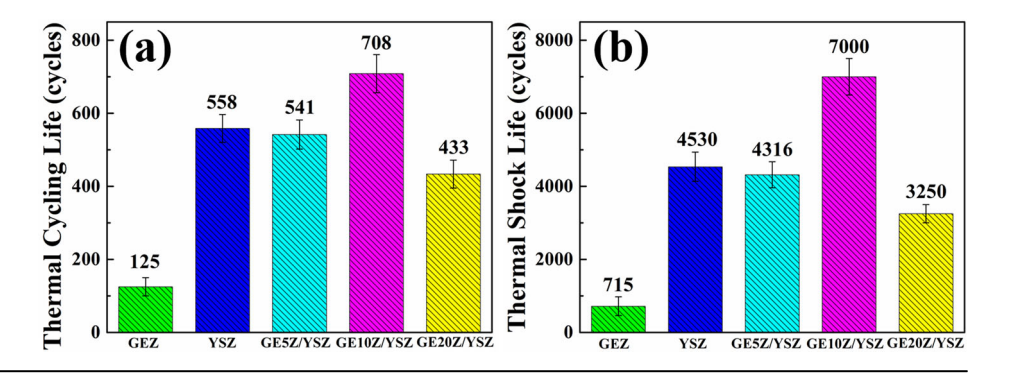
As show in Fig. 5, the hierarchical microstructure of the GE10Z top layer is characterized using TEM, high-resolution transmission electron microscopy (HRTEM), and fast Fourier transform (FFT). Figure 5a, b reveals an evident feathery structure with internal gaps and linear pores in the column. A closer examination of the HRTEM image, as shown in Fig. 5c, discloses that the crystal spacing within the GE10Z top layer measures approximately 0.268 nm and 0.192 nm, corresponding to the (200) and (220) planes of $Gd_2Zr_2O_7$, respectively. Upon a clear observation of the FFT of the columnar tips (located at the top left corner of Fig. 5c), the lattice structure is seen to exhibit a fluorite structure. The lattices in the FFT are associated with the [100] zone axis, suggesting that the fluorite structure predominantly features a large (200) plane area in the GE10Z coatings. This

observation implies that the feathery structure is likely formed by a structure-temperature relationship where the substrate temperature ($T_{substrate}$) is within the range of 0.3 $T_{\rm m}$ to 0.5 $T_{\rm m}$ (with $T_{\rm m}$ for GdEuZrO being approximately 2273 K). These feathery structures are hypothesized to confer a high degree of strain tolerance during thermal cycling tests. Furthermore, the feathery microstructure, characterized by internal gaps and linear pores, is also expected to significantly influence the thermal conductivity of the material.

Thermal durability

To assess the potential application of these TBCs systems, we evaluated the thermal durability of GEZ single coatings, YSZ single coatings, GE5Z/YSZ, GE10Z/YSZ, and GE20Z/YSZ double layer coatings under identical conditions. NiCoCrAlYHf coatings of uniform thickness were employed as bonding layers. The average lifetime of the TBCs was determined based on the performance of five samples. As illustrated in Fig. 6, the GE10Z/YSZ TBCs demonstrated the longest lifetime, achieving 708 cycles, in contrast to the YSZ TBCs, which lasted 558 cycles, and the GEZ single TBCs, which only reached 125 cycles. Furthermore, the GE10Z/YSZ TBCs also demonstrated the longest lifetime, in contrast to the GE5Z/YSZ TBCs, which lasted 541 cycles, and the GE20Z/YSZ TBCs, which only reached 433 cycles. Additionally, to analyze the heating and cooling processes, we compared the thermal shock lifetimes of the TBCs, as shown in Fig. 6b. The GE10Z/YSZ TBCs again outperformed the others, exhibiting a thermal shock lifetime of 7000 cycles, compared to 4530 cycles for YSZ TBCs, 715 cycles for GEZ single TBCs, 4316 cycles for GE5Z/YSZ TBCs, and 3250 cycles for GE20Z/ YSZ TBCs. Overall, both the thermal cycling lifetime and the thermal shock lifetime of the GE10Z/YSZ TBCs indicate a significant enhancement in

Fig. 6 | Thermal durability of the as-deposited GEZ, YSZ, GE5Z/YSZ, GE10Z/YSZ and GE20Z/YSZ TBCs. a Thermal cycling lifetime; (b) thermal shock lifetime.



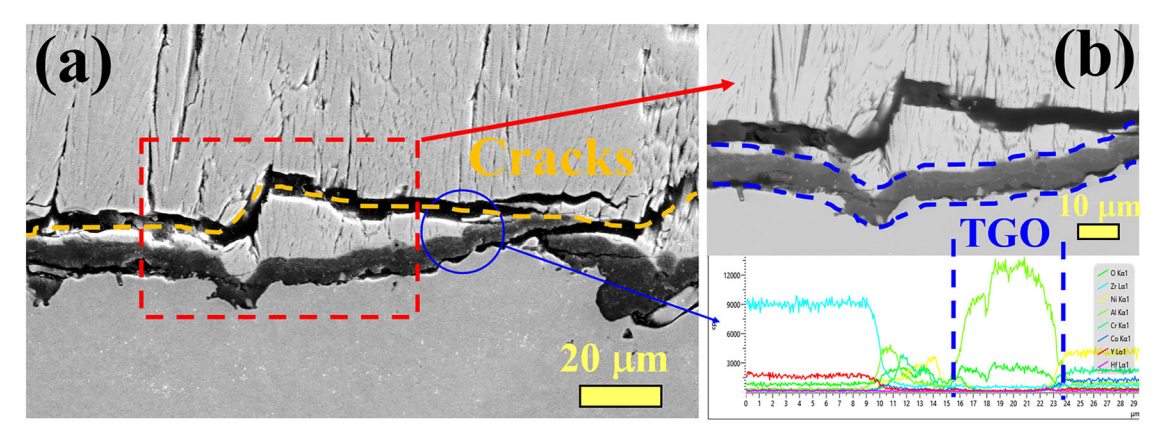


Fig. 7 | Cross-section morphology after thermal cycling test. a Cross-section of TBCs; (b) Cross-section and EDS line scans of TGO layer and YSZ/NiCoCrAlYHf interface.

Table 1 | The thickness of TGO layer in the GE10Z/YSZ/ NiCoCrAlYHf, YSZ/NiCoCrAlYHf and GE10Z/NiCoCrAlYHf system

Sample	Thickness (µm)
GE10Z/YSZ/NiCoCrAlYHf	7–9
YSZ/NiCoCrAlYHf	5–7
GE10Z/NiCoCrAlYHf	8–10

thermal durability. The enhanced thermal performance of GE10Z/YSZ TBCs primarily stems from GE10Z's high thermal expansion coefficient, which improves compatibility with the substrate and NiCoCrAlYHf bond coat $^{1-3}$. Furthermore, optimized europium doping might enhance the high-temperature phase stability of $\rm Gd_2Zr_2O_7$, contributing to good thermomechanical properties 5,6 .

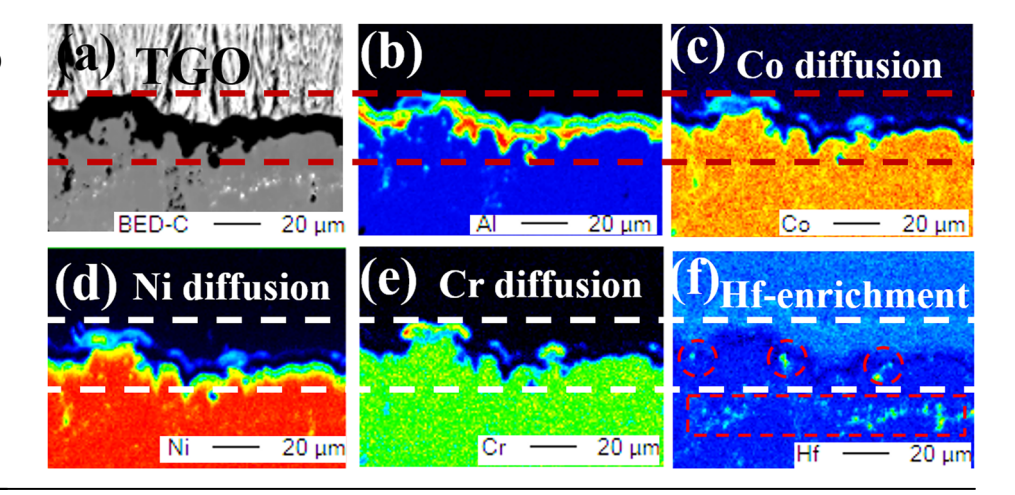
The thermal durability results suggest that the GEZ/YSZ double layer is a promising candidate for high-temperature applications in gas turbines and other thermal environments. The enhanced thermal durability of GEZ/YSZ TBCs can be attributed to several key factors as following: (1) The appropriate incorporation of Eu into $Gd_2Zr_2O_7$ results in a stabilized solid solution that exhibits excellent thermal stability. The appropriate substitution of Eu for Gd in $Gd_2Zr_2O_7$ introduces complex point defects, which enhance the resistance to sintering of the top layer, thereby contributing to a longer service lifetime. (2) The higher TEC of the GEZ top layer helps to minimize the TEC mismatch between the GEZ layer, the YSZ layer, and the NiCo-CrAlYHf layer. The dual-layer design, with YSZ as the intermediate ceramic layer between the GEZ top layer and the NiCo-CrAlYHf layer, further reduces thermal stress caused by TEC mismatch. This reduction in thermal stress is beneficial for alleviating the thermal stresses that arise between the ceramic top layer, YSZ layer, NiCoCrAlYHf layer, and substrate, leading to

an increased thermal lifetime of the TBCs^{6–10}. (3) The feathery microstructure, characterized by internal gaps and linear pores, significantly influences the adhesive strength, strain tolerance, and compliance of the asdeposited TBCs. These structural features are crucial for managing residual stresses and enhancing the overall lifetime of the TBCs. (4) The lower thermal conductivity of the GEZ layer provides improved thermal insulation for the NiCoCrAlYHf layer and the substrate. The double layer design of GEZ + YSZ also creates a temperature gradient during the heating process, which is advantageous for the thermal protection of the underlying layers. In conclusion, the substitution effect of Eu, the elevated TEC, the unique feathery microstructure, and the reduced thermal conductivity are the four main contributors to the superior thermal lifetime of GEZ/YSZ TBCs. These attributes make them an excellent choice for applications in gas-turbine engines, where high thermal and mechanical stability are essential.

Failure behavior

To assess the failure mechanisms of multi-layer TBCs, the development and progression of the TGO and ceramic layers were examined using SEM, EDS line scans, and EPMA. As shown in Fig. 7a, the TBCs system is composed of three layers: the YSZ layer, the TGO layer, and the NiCoCrAlYHf bond coat layer. The expansion of the TGO layer leads to the accumulation of thermal stresses within the TBCs. The growth and thickening of the TGO layer are correlated with the initiation and propagation of cracks. Upon completion of the thermal cycling test, the TGO layer's thickness of GE10Z/YSZ/NiCoCrAlYHf reached approximately 7–9 μm . Furthermore, the TGO evolution of YSZ/NiCoCrAlYHf TBCs and GE10Z/NiCoCrAlYHf TBCs has also been investigated under the same conditions. As shown in Fig. S1 and Table 1, the TGO layer's thickness of YSZ/NiCoCrAlYHf TBCs reached approximately 5-7 μm , and the TGO layer's thickness of GE10Z/NiCoCrAlYHf TBCs reached approximately 8-10 μm . In the open literature, the

Fig. 8 | Cross-section of TGO layer and corresponding EPMA maps. a cross-section; (b) Al; (c) Co; (d) Ni; (e) Cr; (f) Hf.



TGO layer in TBCs systems typically reaches a thickness of 6-10 μ m by the end of thermal durability tests. This range aligns with observed TGO evolution in GE10Z/YSZ/NiCoCrAlYHf, GE10Z/NiCoCrAlYHf, and YSZ/NiCoCrAlYHf TBCs systems 1,2,10 .

To delve into the elemental composition of the TGO layer, EDS line scans were conducted at the boundary between the YSZ and NiCoCrAlYHf layers. Figure 7b illustrates the SEM analysis of the TGO layer and its interface. The bottom figure in Fig. 7b shows the EDS line scans, where the green line indicates the presence of Al element. Consequently, the dark layer, rich in Al and O, is identified as the TGO layer, primarily composed of aluminum oxide (Al₂O₃). Furthermore, no chipping or failure occurred in the GE10Z layers in the TBCs system. The primary failure mode remained TGO-driven at interface. Additionally, the valleys in the EDS line scan correspond to the locations of the cracks. Throughout the thermal cycling process, thermal stresses accumulate and are released within the TBCs, leading to the formation of horizontal cracks at the YSZ-TGO interface. At the end of thermal cycling test, these cracks had interconnected, forming a large-scale network. The coalescence of cracks results in a separation zone, causing damage to the columnar grains near the TGO layer, to a depth of about 3-5 μm. Moreover, bright spots were observed within the TGO layer and at the interface with the bond coat. These spots may indicate the formation of new phases or compounds. Furthermore, the failure behaviors of YSZ/NiCoCrAlYHf TBCs and GE10Z/NiCoCrAlYHf TBCs have also been investigated under the same conditions. As shown in Fig. S1, the main cause of failure of YSZ/NiCoCrAlYHf TBCs is TGO evolution. When the TGO thickness in YSZ/NiCoCrAlYHf TBCs reaches the critical thickness (approximately 5-7 µm), the YSZ/NiCoCrAlYHf TBCs would fail and break. On the other hand, the main cause of the failure of GE10Z/NiCo-CrAlYHf TBCs is TGO and crack evolution. As shown in Fig. S1, the coalescence of cracks results in a separation zone, causing damage to the columnar grains near the TGO layer and even destroying the GEZ layer. Overall, the degradation of thermal stability is primarily due to the evolution of cracks under high-temperature conditions.

To delve deeper into the elemental evolution and the failure mechanism, EPMA images of the YSZ/TGO/NiCoCrAlYHf interface were examined following the thermal cycling experiment. Figure 8a illustrates the growth of the TGO layer, which is particularly evident at the interface between the YSZ and TGO layers. Figures 8b through 8f depict the distribution of Al, Co, Ni, Cr, and Hf elements, respectively. Figure 8b reveals that Al is predominantly found within the TGO layer. Figure 8c–e shows that Co, Ni, and Cr are primarily located in the NiCoCrAlYHf layer. After the thermal cycling test, it is observed that some of the bond coat layer elements (Co, Ni, and Cr) have diffused and concentrated within the TGO layer. Figure 8f highlights the presence of bright spots within the TGO layer, indicating that Hf from the NiCoCrAlYHf layer has diffused outward, creating an Hf-enriched region.

At high temperatures (1150 °C), the outward diffusion of elements leads to the formation and growth of Ni-Cr-Co-Al-Hf oxides within the TGO layer^{43–48}. The emergence of these oxides could result in the introduction of new phases and compounds. Consequently, the bright spots detected within the TGO layer are attributed to this phenomenon. The formation of Ni-Cr-Co-Al-Hf oxides may also cause volume changes during the thermal cycling test due to the thermal expansion coefficient mismatch. These volume changes can induce crack formation and coalescence within the TBCs. Moreover, the TEC mismatch between the newly formed Ni-Cr-Co-Al-Hf oxides and the rest of the TBCs system can lead to interface instability during the heating and cooling cycles. In summary, elemental diffusion and the evolution of cracks are two primary contributors to the failure mechanism of GE10Z/YSZ TBCs. Understanding the progression of thermal properties and failure behavior in GE10Z/YSZ TBCs can offer valuable insights for the development of other advanced TBC systems.

In conclusion, the GdEuZrO and YSZ layers were applied using EB-PVD, while the NiCoCrAlYHf layer was deposited via PVD technology. The TBCs system comprises a GdEuZrO top ceramic layer, an intermediate YSZ ceramic layer, and a NiCoCrAlYHf metallic bottom layer. The phase structure of both the GdEuZrO ingot and the TBCs is characterized by a Fm-3m cubic fluorite structure. The TEC of GdEuZrO, ranging from $10.72*10^{-6} \text{ K}^{-1}$ to $11.49*10^{-6} \text{ K}^{-1}$, significantly exceeds that of $Gd_2Zr_2O_7$ and YSZ. The GE10Z exhibits a thermal conductivity of 1.280 W/mK at 1000 °C, which is notably lower than that of YSZ. The GdEuZrO layer's column tips reveal a distinct feathery morphology interspersed with internal gaps and linear pores. The GE10Z/YSZ TBCs demonstrate superior thermal shock resistance, enduring up to 7000 cycles, and a thermal cycling lifetime of 708 cycles, surpassing the performance of both YSZ TBCs and GEZ TBCs. The high TEC of GdEuZrO, the feathery microstructure, the low thermal conductivity, and the substitution effect of Eu are four key contributors to the enhanced thermal durability of the TBCs. After thermal cycling testing, diffusion and concentration of Ni, Co, Cr, and Hf elements within the TGO layer result in the formation of Ni-Cr-Co-Al-Hf oxides. The TEC mismatch between these Ni-Cr-Co-Al-Hf oxides and the TGO layer can trigger the development and expansion of interfacial instabilities. The migration of elements and the progression of cracks are identified as the primary causes of failure in the GdEuZrO/YSZ TBCs.

Methods

Ingot synthesis

In the standard preparation process, NiCoCrAlYHf ingots were crafted through vacuum melting, which involved the high-purity metals: nickel (99.9%), cobalt (99.9%), chromium (99.9%), aluminum (99.9%), yttrium (99%), and hafnium (99.9%). For the ceramic components, YSZ and gadolinium europium zirconate (GdEuZrO, abbreviated as GEZ) ingots were produced through a solid-state reaction. This process took place at a

temperature of 1973K for 20 hours. The starting materials used for this reaction were of high purity: gadolinium oxide (Gd_2O_3 , 99.9%), europium oxide (Eu_2O_3 , 99.9%), zirconium dioxide (ZrO_2 , 99.9%), and yttrium oxide (Y_2O_3 , 99%). Notably, europium, a rare earth element, was doped into the GdEuZrO ingot at a concentration of 5, 10, and 20 atomic percent, which is expected to influence the material's thermal properties. The abbreviation of GE5Z, GE10Z, and GE20Z correspond to the respective chemical compositions ($Gd_{0.95}Eu_{0.05})_2Zr_2O_7$, ($Gd_{0.9}Eu_{0.1})_2Zr_2O_7$ and ($Gd_{0.8}Eu_{0.2})_2Zr_2O_7$, respectively. The prepared YSZ and GEZ ingots were then cut to a specific size of Φ 68.5 mm × 50.0 mm to fit the requirements of the coating process.

TBCs deposition

The Ni-based superalloy substrate (25.0 mm \times 10.0 mm \times 1.0 mm) was subjected to water grit blasting to enhance surface adhesion prior to depositing a NiCoCrAlYHf coating. Its nominal chemical composition (in wt%) was: 12.5% Co, 6.3% W, 5.7% Ta, 6.3% Al, 2.2% Re, 5.8% Cr, 1.3% Mo, 0.02% C, with Ni as the balance. The NiCoCrAlYHf coating was applied utilizing physical vapor deposition (PVD) technology with equipment model A-1000 from Russia. The deposition process occurred at a temperature of roughly 600 ± 50 °C, and the coating's growth rate was approximately 0.35 micrometers per minute. The NiCoCrAlYHf coatings were heat-treated in a vacuum at 850 ± 50 °C for 3 ± 1.0 h to enhance element diffusion (using a VBF-30 furnace, manufactured in China). Following this, the YSZ and GEZ layers were consecutively deposited using a commercial EB-PVD system, model UE-207S by ICEBT. The respective growth rates for these layers were 5.0 micrometers per minute for YSZ and 3.0 micrometers per minute for GEZ. The deposition process of YSZ and GEZ layers occurred at a temperature of roughly 900 ± 50 °C. All the TBCs exhibited comparable porosity (10 ± 2%) under identical EB-PVD processing conditions. After EB-PVD deposition process, the atomic ratios of Gadolinium (Gd), Europium (Eu), and Zirconium (Zr) in the GZ, GE5Z, GE10Z, and GE20Z coatings are approximately 1.00:0:1.00, 0.98:0.06:1.00, 0.92:0.12:1.00, and 0.78:0.23:1.00, respectively.

Characterization

The phase composition and crystal structure of the coatings and ingots are examined using X-ray diffraction (XRD). The Bruker D8 Advance XRD system, equipped with Cu Ka radiation, is utilized for this purpose with a step size of 5°/min in the 2θ range of 20° – 90° . The concentration of metals within the coatings was ascertained using inductively coupled plasmaatomic emission spectrometry (ICP-AES) on an Agilent 725-ES instrument. The cross-sectional structure of the TBCs is observed using a scanning electron microscope (SEM, FEI-Quanta 600). SEM provides highresolution images of the cross-section morphology and can reveal details such as the columnar structure, porosity, and any defects or cracks in the TBCs. The chemical composition of the TBCs is analyzed using an electron probe micro-analysis (EPMA, JXA-8100 prototype) system with wavelength dispersive spectroscopy (WDS). For a more detailed examination of the microstructure, transmission electron microscopy (TEM, JEM-2100F) is employed. The thermal expansion behavior of the ceramics is measured using a dilatometer (Netzsch DIL 402 C) in the temperature range of 500°-1500°. The dimensions of the bulk ceramic material used for the thermal expansion coefficient (TEC) measurement are 20.0 mm by 5.0 mm by 5.0 mm. The thermal diffusivity (α) of the ceramics, which is a measure of a material's ability to conduct heat, is determined using a laser flash analyzer (Netzsch LFA 427) in the temperature range of 30°-1200°. The bulk ceramic material, intended for thermal diffusivity testing, has a diameter of 10.0 mm and a height of 1.5 mm. To enhance the accuracy of thermal measurements, a thin layer of graphite is applied to both surfaces of the bulk ceramic samples. This application improves the absorption and emission properties of the ceramic, ensuring more reliable measurements of thermal diffusivity. The thermal conductivity (λ) of GEZ and YSZ ceramics can be ascertained through their thermal diffusivity (α), specific heat capacity (Cp), density (ρ), and fractional porosity (φ) . The laser-flash method stands as the predominant technique for assessing thermal diffusivity. Utilizing the following

Table 2 | The fractional porosity of the GdEuZrO and YSZ ceramics

Sample	Porosity (%)
GE5Z	2.3
GE10Z	3.2
GE20Z	4.1
GZ	1.5
YSZ	1.0

equations, the thermal conductivities of GEZ and YSZ ceramic materials were established:

$$\lambda = \rho \times \alpha \times C_p \tag{1}$$

$$\lambda/\lambda_0 = 1 - 4/3\varphi \tag{2}$$

As shown in Table 2, the fractional porosity GE5Z, GE10Z, GE20Z, GZ and YSZ is 2.3%, 3.2%, 4.1%, 1.5% and 1.0%, respectively. In the TBCs system, the density (ρ) of the materials is typically determined using the Archimedes Principle, which relies on the displacement of fluid by the material and is a reliable method for measuring the volume and density of ceramics. The specific heat capacity (Cp) is often ascertained using the Neumann-Kopp rule, which is a generalization that allows for the estimation of the specific heat capacity of a compound based on the properties of its constituent elements $^{10-12}$.

The thermal cycling and thermal shock tests are crucial for evaluating the durability and performance of TBCs under high temperature condition. The furnace temperature was maintained at 1150 °C under ambient atmospheric conditions. The TBCs samples reached the target temperature within approximately 1 minute, corresponding to an average heating rate of 20 °C/s. All TBCs exhibited comparable thicknesses (±5%) when deposited under identical processing conditions. In the thermal cycling test, the TBCs are subjected to a cycle that involves exposure at a high temperature of 1150 °C for a dwell time of 55 minutes. This period of exposure mimics the prolonged high-temperature environment that the TBCs would face in applications such as gas turbine engines. Following the high-temperature exposure, the TBCs are air-cooled for 5 minutes. Air cooling simulates the rapid temperature drop that can occur when a component is exposed to the atmosphere after being in a high-temperature environment. Similar to the thermal cycling test, the TBCs are exposed to 1150 °C but for a shorter dwell time of 5 minutes for thermal shock test. This shorter exposure is designed to assess the TBCs' response to rapid heating. The TBCs are then air-cooled for 5 minutes to quickly reduce the temperature, simulating a thermal shock scenario. The thermal shock test is more severe than the thermal cycling test due to the shorter time at high temperature, which can cause more significant thermal stresses in the coating. After the thermal cycling and thermal shock tests, the temperature of TBCs samples was about 300 ± 50 °C at the end of one cycle. The thermal tests are repeated for a set of TBCs samples, typically five, to ensure statistical reliability and to account for variability in the coating process or material properties. The lifetime of the TBCs is determined by calculating the average number of cycles to failure (10% delamination) across the set of tested samples. The TGO thickness was determined through five independent measurements conducted along the oxide growth direction (normal to the interface). The TGO layer was identified as the gray-black region in cross-sectional micrographs (top interface: transition from YSZ-gray to TGO-black, bottom interface: further color change at the TGO/BC boundary). The reported TGO thickness represents the range of these five perpendicular measurements. In addition, the average value number of cycles is a key performance indicator for the TBCs and is used to compare different coating systems or to assess the impact of changes in coating materials or processes. These tests are essential for predicting the service life of TBCs and for improving their design and

materials to enhance their resistance to thermal fatigue and thermal shock. The data obtained from these tests can be used to optimize coating systems for specific applications, ensuring that they can withstand the rigors of high-temperature service environments.

Data availability

Data that support the findings presented in this manuscript can be provided upon reasonable request by contacting the corresponding author.

Received: 19 February 2025; Accepted: 24 April 2025; Published online: 08 May 2025

References

- Padture, N. P., Gell, M. & Jordan, E. H. Thermal barrier coatings for gas-turbine engine applications. Science 296, 280–284 (2002).
- Clarke, D. R., Oechsner, M. & Padture, N. P. Thermal-barrier coatings for more efficient gas-turbine engines. MRS Bull. 37, 891–898 (2012).
- Levi, C. G. Emerging materials and processes for thermal barrier systems. Curr. Opin. Solid State Mater. Sci. 8, 77–91 (2002).
- Vaßen, R., Jarligo, M. O., Steinke, T. & Mack, D. E. Overview on advanced thermal barrier coatings. Surf. Coat. Technol. 205, 938–942 (2010).
- Sampath, S., Schulz, U., Jarligo, M. O. & Kuroda, S. Processing science of advanced thermal-barrier systems. MRS Bull. 37, 903–910 (2012).
- Pollock, T. M., Lipkin, D. M. & Hemker, K. J. Multifunctional coating interlayers for thermal-barrier systems. MRS Bull. 37, 923–931 (2012).
- Zhao, M. et al. Defect engineering in development of low thermal conductivity materials: a review. J. Eur. Ceram. Soc. 37, 1–13 (2017).
- Dong, S. J. et al. Thermal radiation and cycling properties of (Ca, Fe) or (Sr, Mn) co-doped La₂Ce₂O₇ coatings. *J. Eur. Ceram. Soc.* 40, 2020–2029 (2020).
- Shen, Z. Y. et al. Effects of Er stabilization on thermal property and failure behavior of Gd₂Zr₂O₇ thermal barrier coatings. *Corros. Sci.* 185, 109418 (2021).
- Mahade, S. et al. Functional performance of Gd₂Zr₂O₇/YSZ multilayered thermal barrier coatings deposited by suspension plasma spray. Surf. Coat. Technol. 318, 208–216 (2017).
- Gok, M. G. & Goller, G. Production and characterization of GZ/CYSZ alternative thermal barrier coatings with multilayered and functionally graded designs. J. Eur. Ceram. Soc. 36, 1755–1764 (2016).
- Shen, Z. Y. et al. LaGdZrO/YSZ thermal barrier coatings by EB-PVD: Microstructure, thermal properties and failure mechanism. *Chem. Eng. J. Adv.* 5, 100073 (2021).
- Shen, Z. Y., He, L. M., Xu, Z. H., Mu, R. D. & Huang, G. H. Morphological evolution and failure of LZC/YSZ DCL TBCs by electron beam-physical vapor deposition. *Materialia* 4, 340–347 (2018).
- Shen, Z. Y., He, L. M., Xu, Z. H., Mu, R. D. & Huang, G. H. LZC/YSZ DCL TBCs by EB-PVD: Microstructure, low thermal conductivity and high thermal cycling life. *J. Eur. Ceram. Soc.* 39, 1443–1450 (2019).
- Shen, Z. Y., He, L. M., Xu, Z. H., Mu, R. D. & Huang, G. H. Effects of gradient transitional layer on thermal cycling life and failure of LaZrCeO/YSZ thermal barrier coatings. *Corros. Sci.* 163, 108224 (2020).
- Yan, S. L. et al. HVOF-sprayed AlSi50 alloy coatings as a novel electrothermal anti-icing/de-icing system for polymer-based composite structures. J. Therm. Spray. Techn. 30, 2161–2173 (2021).
- Shen, Z. Y., He, L. M., Xu, Z. H., Mu, R. D. & Huang, G. H. Rare earth oxides stabilized La₂Zr₂O₇ TBCs: EB-PVD, thermal conductivity and thermal cycling life. Surf. Coat. Technol. 357, 427–432 (2019).
- Wan, C. L., Qu, Z. X., Du, A. & Pan, W. Influence of B site substituent Ti on the structure and thermophysical properties of A₂B₂O₇-type pyrochlore Gd₂Zr₂O₇. Acta Mater. 57, 4782–4789 (2009).

- Bahamirian, M., Hadavi, S. M. M., Farvizi, M., Rahimipour, M. R. & Keyvani, A. Phase stability of ZrO₂ 9.5Y₂O₃ 5.6Yb₂O₃ 5.2Gd₂O₃ compound at 1100 °C and 1300 °C for advanced TBC applications. *Ceram. Int.* 45, 7344–7350 (2019).
- Song, D. et al. Hot-corrosion resistance and phase stability of Yb₂O₃-Gd₂O₃-Y₂O₃ costabilized zirconia-based thermal barrier coatings against Na₂SO₄+V₂O₅ molten salts. Surf. Coat. Technol. 400, 126 (2020).
- Zhang, X. F. et al. Gas-deposition mechanisms of 7YSZ coating based on plasma spray-physical vapor deposition. *J. Eur. Ceram. Soc.* 36, 697–703 (2015).
- Zhou, X. et al. Failure of plasma sprayed nano-zirconia-based thermal barrier coatings exposed to molten CaO-MgO-Al₂O₃-SiO₂ deposits. J. Am. Ceram. Soc. 102, 6357–6371 (2019).
- Shen, Z. Y., Liu, G. X., He, L. M., Mu, R. D. & Dai, J. W. Thermal property and failure behaviors of Gd doped LaZrCeO coatings with feathery microstructure. *npj Mater. Degrad.* 6, 17 (2022).
- Zhou, X. et al. Thermophysical properties and cyclic lifetime of plasma sprayed SrAl12O19 for thermal barrier coating applications. *J. Am. Ceram. Soc.* 103, 5599–5611 (2020).
- Levi, C. G., Hutchinson, J. W., Vidal-Sétif, M. & Johnson, C. A. Environmental degradation of thermal barrier coatings by molten deposits. MRS Bull. 37, 932–941 (2012).
- 26. Pan, W., Phillpot, S. R., Wan, C. L., Chernatynskiy, A. & Qu, Z. X. Low thermal conductivity oxides. *MRS Bull.* **37**, 917–922 (2012).
- Shen, Z. Y. et al. Thermal property and failure behavior of LaSmZrO thermal barrier coatings by EB-PVD. iScience 25, 104106 (2022).
- Li, Y. R., Wang, J. M. & Wang, J. Y. Theoretical investigation of phonon contributions to thermal expansion coefficients for rare earth monosilicates RE₂SiO₅ (RE = Dy, Ho, Er, Tm, Yb and Lu). *J. Eur. Ceram. Soc.* 40, 2658–2666 (2020).
- Ortalan, V., Uzun, A., Gates, B. C. & Browning, N. D. Towards fullstructure determination of bimetallic nanoparticles with an aberrationcorrected electron microscope. *Nat. Nanotech.* 5, 843–847 (2010).
- Muller, D. A. Structure and bonding at the atomic scale by scanning transmission electron microscopy. *Nat. Mater.* 8, 263–270 (2009).
- Shen, Z. Y. et al. Thermal property and failure behaviour of Pr doped Gd₂Zr₂O₇ thermal barrier coatings. Corros. Sci. 226, 111641 (2024).
- Vaßen, R., Kagawa, Y., Subramanian, R., Zombo, P. & Zhu, D. M. Testing and evaluation of thermal-barrier coatings. MRS Bull. 37, 911–916 (2012).
- Liu, D., Rinaldi, C. & Flewitt, P. E. J. Effect of substrate curvature on the evolution of microstructure and residual stresses in EBPVD-TBC. *J. Eur. Ceram. Soc.* 35, 2563–2575 (2015).
- Jonnalagadda, K. P. et al. A study of damage evolution in high purity nano TBCs during thermal cycling: a fracture mechanics based modelling approach. J. Eur. Ceram. Soc. 37, 2889–2899 (2017).
- 35. Shen, Z. Y. et al. Thermal property and failure mechanism of LaDyZrO thermal barrier coatings by electron beam physical vapor deposition. *Mater. Today Phys.* **24**, 100696 (2022).
- Shen, Z. Y. et al. Thermal shock life and failure behaviors of La₂Zr₂O₇/ YSZ, La₂Ce₂O₇/YSZ and Gd₂Zr₂O₇/YSZ DCL TBCs by EB-PVD. Mater. Charact. 173, 110923 (2021).
- Shen, Z. Y., He, L. M., Xu, Z. H., Mu, R. D. & Huang, G. H. LZC/YSZ double layer coatings: EB-PVD, microstructure and thermal cycling life. Surf. Coat. Technol. 357, 427–432 (2019).
- 38. Che, J. W., Wang, X. Z., Liu, X. Y., Liang, G. Y. & Zhang, S. L. Thermal transport property in pyrochlore-type and fluorite-type A2B2O7 oxides by molecular dynamics simulation. *Int. J. Heat. Mass Tran.* **182**, 122038 (2022).
- Yang, J. et al. Diffused lattice vibration and ultralow thermal conductivity in the binary Ln-Nb-O oxide system. *Adv. Mater.* 31, 1808222 (2019).
- Yu, B. et al. Evolution of cold-expanded microstructure with aging temperature and its influence on fatigue performance of hole structure at elevated temperature. J. Alloy. Compd. 970, 172562 (2024).

- Shen, Z. Y. et al. Effect of Er on thermal property and failure behaviour of LaErZrO thermal barrier coatings. Corros. Sci. 209, 110749 (2022).
- Chen, Y., Zhao, X. F. & Xiao, P. Effect of microstructure on early oxidation of MCrAlY coatings. Acta Mater. 159, 150—1162 (2018).
- Chen, Y. et al. A mechanistic understanding on rumpling of a NiCoCrAlY bond coat for thermal barrier coating applications. *Acta Mater.* 128, 31–42 (2017).
- Yang, L. X. et al. High temperature stress and its influence on surface rumpling in NiCoCrAlY bond coat. Acta Mater. 139, 122–137 (2017).
- 45. Tolpygo, V. K., Murphy, K. S. & Clarke, D. R. Effect of Hf, Y and C in the underlying superalloy on the rumpling of diffusion aluminide coatings. *Acta Mater.* **56**, 489–499 (2008).
- Evans, A. G., Mumm, D. R., Hutchinson, J. W., Meier, G. H. & Pettit, F. S. Mechanisms controlling the curability of thermal barrier coatings. *Prog. Mater. Sci.* 46, 505–553 (2001).
- Ghadami, F., Aghdam, A. S. R. & Ghadami, S. Microstructural characteristics and oxidation behavior of the modified MCrAIX coatings: A critical review. *Vacuum* 185, 109980 (2021).
- Evans, A. G., Clarke, D. R. & Levi, C. G. The influence of oxides on the performance of advanced gas turbines. *J. Eur. Ceram. Soc.* 28, 1405–1419 (2008).

Acknowledgements

This research was financially supported by the National Natural Science Foundation of China, grant number 52202073.

Author contributions

Zaoyu Shen analyzed and interpreted thermo-physical properties and failure behavior and was a major contributor in writing the manuscript. Yuqing Luo analyzed and discussed the microstructure characterization of TBCs. Guanxi Liu analyzed and discussed thermo-physical property. Jianwei Dai analyzed and discussed thermal durability. Limin He analyzed and interpreted the failure behavior of TBCs. Rende Mu analyzed and discussed failure behavior and thermal durability. All authors reviewed the manuscript. All authors read and approved the final manuscript.

Competing interests

The authors declare no competing interests.

Additional information

Supplementary information The online version contains supplementary material available at https://doi.org/10.1038/s41529-025-00598-3.

Correspondence and requests for materials should be addressed to Zaoyu Shen or Rende Mu.

Reprints and permissions information is available at http://www.nature.com/reprints

Publisher's note Springer Nature remains neutral with regard to jurisdictional claims in published maps and institutional affiliations.

Open Access This article is licensed under a Creative Commons Attribution-NonCommercial-NoDerivatives 4.0 International License, which permits any non-commercial use, sharing, distribution and reproduction in any medium or format, as long as you give appropriate credit to the original author(s) and the source, provide a link to the Creative Commons licence, and indicate if you modified the licensed material. You do not have permission under this licence to share adapted material derived from this article or parts of it. The images or other third party material in this article are included in the article's Creative Commons licence, unless indicated otherwise in a credit line to the material. If material is not included in the article's Creative Commons licence and your intended use is not permitted by statutory regulation or exceeds the permitted use, you will need to obtain permission directly from the copyright holder. To view a copy of this licence, visit http://creativecommons.org/licenses/by-nc-nd/4.0/.

© The Author(s) 2025